PIER M

Magneto-Acousto-Electrical Tomography Based on Synthetic Aperture with Inhomogeneous Static Magnetic Field

Shuaiyu Bu[1,2,3], Xingchen Zhang[4], Sanxi Wu[1,2], Guoqiang Liu[1,2], Wenting Ren[5], and Yuanyuan Li[1,2,*]

[1]*Institute of Electrical Engineering, Chinese Academy of Sciences, Beijing 100190, China*
[2]*School of Electronic Electrical and Communication Engineering, University of Chinese Academy of Sciences*
Beijing 100049, China
[3]*State Grid Beijing Electric Power Company, Beijing 100031, China*
[4]*Shandong University of Science and Technology, Qingdao, China*
[5]*Department of Radiation Oncology, National Cancer Center/National Clinical Research Center for Cancer/Cancer Hospital*
Chinese Academy of Medical Sciences and Peking Union Medical College, China

ABSTRACT: Magneto-acousto-electrical tomography (MAET) is an imaging method generating a source current under the excitation of both static magnetic field and acoustic field, and electrodes are used to detect the electrical signal to further reconstruct conductivity image. Previous studies ignored the non-uniformity of magnetic field. However, the reconstructed image will introduce artifacts due to magnetic field inhomogeneity, which is small but cannot be neglected. We analyzed the characteristics of magneto-acousto-electrical signal under uniform and inhomogeneous magnetic fields in simulation. This paper deduces the relation of magneto-acoustic signal generated by inhomogeneous static magnetic field and reconstructed conductivity image under nonuniform static magnetic field through synthetic aperture imaging. Furthermore, to verify the validity of the theory, an experimental platform was built to reconstruct the conductivity of phantom. In clinical applications, nonuniform static magnetic field can achieve a fully open magnetic field structure, which is much more friendly for the inspection of patients with autism and even children. Permanent magnets that generate nonuniform static magnetic fields have the advantages of smaller size, lighter weight, and lower cost than magnets that generate uniform static magnetic field, which can effectively optimize equipment space.

1. INTRODUCTION

Since changes in physiological and pathological states can lead to edema and different water contents in tissues, the electrical impedances of two states are different, thereby affecting characteristics of electrical impedance [1]. In theory, physiological and pathological states can be distinguished by measuring electrical parameters. In previous studies, changes in electrical characteristics of tissues can be observed earlier than lesions in tissue structure [2]. Therefore, the imaging method of electrical parameters holdd promise for early detection of tumors [3]. Magneto-acousto-electrical tomography (MAET) is a nondestructive imaging method to detect electrical characteristics of tissues, which has advantages of high contrast, high resolution, sensitivity, and penetration depth [3, 4].

MAET was proposed firstly by Wen et al. at the National Institutes of Health in Bethesda, Maryland, USA. They established the foundation of B-scan imaging by deducing the qualitative relationship between the one-dimensional voltage signal and the conductivity of ultrasonic propagation path. B-scan imaging of bacon was conducted to verify the theory of MAET [4]. Montalibet et al. at the National Institute for Health and Medical Research, Lyon, France processed magneto-acousto-electrical signals with inversing filter, increasing the resolution on horizontal axis to 1 millimeter [6].

Xu et al. in Ryerson University established the quantitative relationship among the measured voltage, equivalent source electric field intensity, and current density based on reciprocity theorem. The current density distribution image of the reciprocity process was also obtained by simulations and experiments [7–10]. Liu's group in the Institute of Electrical Engineering, Chinese Academy of Sciences, realized electrode-detected MAET signal acquisition [11]; the integral equation for the reciprocal field of the coil-detected mode was derived, and the conductivity image of a 16 S/m phantom was reconstructed [12, 13]. Grasland-Mongrain et al. achieved the B-scan imaging of isolated beef in 0.35 T static magnetic field [14]. Kunyansky et al. at the University of Arizona, USA, reconstructed the B-scan imaging of beef tissue with two pairs of electrodes in 0.35 T static magnetic field [15]. He at Shenzhen University reconstructed the B-scan imaging of 5% graphite powder and 1% NaCl phantom with low-frequency signal excitation and Doppler signal detection [16]. Subsequently, the B-scan imaging of 0.4% NaCl phantom was obtained in 0.45 T static magnetic field [17]. Kaboutari et al. increased the static magnetic field to 0.56 T and achieved B-scan imaging of 3 S/m phantom with coils [18]. The research group of Shenzhen University further increased the static magnetic field to 0.77 T using a filtered back-projection algorithm to achieve the conductivity boundary imaging of a 3% NaCl phantom [19]. Liu's group improved the excitation detection mode and reconstructed im-

---

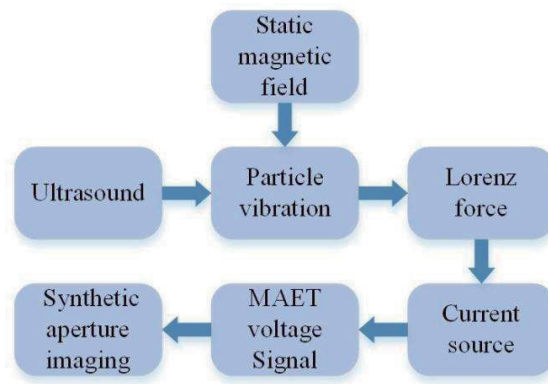* Corresponding author: Yuanyuan Li (lyy@mail.iee.ac.cn).

FIGURE 1. Flow diagram of MAET.

age of 0.2 S/m phantom imaging and pork in 0.26 T static magnetic field with a resolution of 0.5 mm [20–22]. B-scan imaging of isolated mouse liver in 0.3 T static magnetic field was achieved experimentally [23], and B-scan images of lung tissue were reconstructed in simulation [24]. Li et al. used MAET to detect neocrown pneumonia and reconstructed B-scan images by simulating a pre-pulmonary edema or solid lung model and a complete pulmonary edema or solid lung model [24]. Deng et al. improved imaging sensitivity of MAET with Barker coding excitation and reconstructed images of 0.16 S/m phantom and isolated pork tissue in 0.77 T static magnetic field [25]. Li et al. changed the ultrasonic cyclotron radiation pattern and the tilt angle of the conductivity boundary to improve the distortion problem of MAET and verified the findings by applying B-mode to reconstructed images of 1 S/m phantom in experiments [26].

From existing reports and related literature, MAET requires static magnetic field as an excitation source, which is an important component of MAET. At present, studies on MAET always assume that the static magnetic field is uniform. The previous study of MAET with inhomogeneous static magnetic field applying reciprocity theorem achieved a conductivity image and detected target whose conductivity was 4.0 S/m [27]. The design of uniform static magnetic field can refer to the magnetic field in magnetic resonance. However, the realization of a uniform static magnetic field will greatly increase the cost of the uniform permanent magnet, and the cost of clinical application equipment of MAET increases further. In addition, it is hard to obtain a completely uniform static magnetic field in practice. Thus, different from uniform static magnetic field, applying inhomogeneous static magnetic field is closer to reality. Nonuniform static magnetic field can achieve a fully open magnetic field structure, which is much more friendly for the inspection of patients with autism and even children. In addition, applying nonuniform static magnetic field can reduce the cost of equipment in clinic medicine.

The principle of MAET is expressed in Fig. 1. With the excitation of static magnetic field and ultrasound field, ions inside the target body will be subjected to Lorentz force, which further generate dynamic current source, and voltage signals can be detected by electrodes or coils. Then after applying the synthetic aperture method, the MAE images can be reconstructed.

From the theory of MAET, the uniformity of the static magnetic field is not the essential requirement. Static magnetic field and acoustic field interact within the target will generate dynamic current source. As a result, the key point of the problem is how to use MAE signals with synthetic aperture imaging to improve the distortion of the conductivity partition interface brought by the non-uniform static magnetic field.

Previous studies assumed that the magnetic field is uniform, ignoring the image distortion caused by the non-uniformity of magnetic field. In this study, we analyze the characteristics of MAET signals in both uniform static magnetic field and nonuniform static magnetic field. Since the forward problem analysis of electromagnetic field and numerical simulation cannot reflect the change rules of magneto-acoustic signals directly with different static magnetic field excitation, this paper deduces the principle of MAET in inhomogeneous static magnetic field. An equivalent uniform magnetic field adjustment method is proposed. MAET with synthetic aperture in an inhomogeneous static magnetic field was achieved by simulation and experiments. Image distortion was also improved under excitation of non-uniformity magnetic field.

2. THEORY

2.1. MAET

In previous studies of MAET theory, it was always assumed that the magnetic excitation source was uniform, and the influence brought by the inhomogeneity of the static magnetic field was ignored. Accordingly, it is assumed that the magnetic field $\mathbf{B}_0$ is along a certain direction, and the value of $\mathbf{B}_0$ is a constant.

MAET requires the excitation from both sound field and static magnetic field. Ultrasonic waves generated by ultrasonic transducers propagate to the target in static magnetic field. The direction of ultrasonic propagation is perpendicular to the direction of static magnetic field $\mathbf{B}_0$, and the vibration velocity is $\mathbf{v}$.

The ions q in the target are subjected to a Lorentz force in the presence of static magnetic field and acoustic field, which can be expressed as $\mathbf{F} = q\mathbf{v} \times \mathbf{B}_0$. Since the directions of Lorentz force of positive and negative ions in the target are in the same magnitude but in opposite directions, a distributed current is
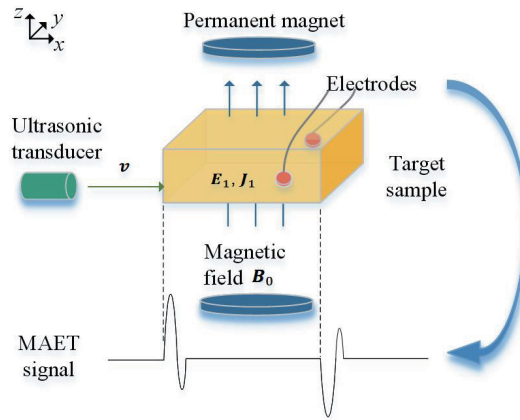
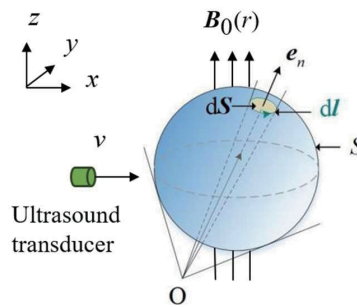**FIGURE 2**. Schematic diagram of MAET.

FIGURE 3. Current source in three-dimensional model.

generated inside the target

$$\mathbf{J}_e = \sigma \mathbf{v} \times \mathbf{B}_0 \qquad (1)$$

where σ is the conductivity of the target body. $\mathbf{J}_e$ is the current density of the equivalent current source.

Wen et al. studied the MAET theory of a one-dimensional model under the excitation of uniform static magnetic field in 1998 and established the qualitative relationship between MAET signal and electrical conductivity [4]. In the simplified one-dimensional model given by them, the static magnetic field $\mathbf{B}_0$ was uniform; the width of the ultrasound propagating beam is W; the direction of the static magnetic field was assumed as $\mathbf{e}_z$; and the ultrasound propagated along the $\mathbf{e}_x$ direction with the vibration speed $\mathbf{v}$, as shown in Fig. 2. Integrating the ultrasonic bandwidth and the current density of the ultrasonic propagating path, the current inside the target can be obtained as

$$I(t) = W B_0 \int_{soundpath} \sigma v(x,t) dx \qquad (2)$$

Further based on the acoustic principle, the expression of the measured voltage of MAET can be obtained by simplification as

$$V(t) = \alpha W B_0 \int_{soundpath} M(x,\tau) \frac{\partial}{\partial x} \left(\frac{\sigma}{\rho_0} \right) dx \qquad (3)$$

where α is the proportionality constant indicating the current detected by the acquisition system; W is the width of the ul-

trasonic beam; M is ultrasound momentum; σ and ρ_0 are the conductivity and density distribution of the target, respectively.

In addition, it can be seen from Equation (3) that only at gradients $\frac{\partial}{\partial x}(\sigma/\rho_0)$, the measured voltage is unequal to zero, the voltage difference between the MAET signals detected by the two electrodes in the surface of the target is not zero. Gradient or boundary of conductivity σ or density ρ_0 can be expressed by the detected voltage. The relationship between the MAET signal and parameters, conductivity, and density, was proposed in this equation. However, there is still an uncertainty term α in this relationship, which means that the relationship can only be used to describe the voltage $V(t)$ proportional to $B_0 \int_{soundpath} M(x,\tau) \frac{\partial}{\partial x}(\frac{\sigma}{\rho_0}) dx$, qualitatively. In this way, the one-dimensional model can be extended to three-dimensional one, and the principle of MAET signals in inhomogeneous static magnetic field can be derived.

For a given three-dimensional model, the current corresponding to the equivalent current source in the target with the excitation of a static magnetic field $\mathbf{B}_0(\mathbf{r})$ shown in Fig. 3 can be expressed as $I(t) = \int_s \sigma \mathbf{v} \times \mathbf{B}_0(\mathbf{r}) \cdot dS$.

From the acoustic principle, the relationship between sound pressure and vibration speed is

$$-\nabla p = \rho_0 \frac{\partial \mathbf{v}}{\partial t} \qquad (4)$$

where ρ_0 is the density of target.

Ultrasound momentum M and sound pressure p are satisfied

$$M = \int_{-\infty}^{t} p d\tau \qquad (5)$$

Taking derivatives of both sides of Equation (6) with respect to time, the following equation is given by

$$\frac{\partial M}{\partial t} = p \qquad (6)$$

Substituting Equation (6) into Equation (4), the relationship between v and M is

$$\mathbf{v} = -\frac{1}{\rho_0}\nabla M \qquad (7)$$

Apply Equation (7) to $I(t) = \int_s \sigma \mathbf{v} \times \mathbf{B}_0(\mathbf{r}) \cdot dS$, the current can be expressed as

$$I(t) = -\int_s \frac{\sigma}{\rho_0}\nabla M \times \mathbf{B}_0(\mathbf{r}) \cdot \mathbf{n} dS \qquad (8)$$

Apply a vector equation $\nabla \times (M\mathbf{B}_0) = \nabla M \times \mathbf{B}_0 + M\nabla \times \mathbf{B}_0$ to Equation (8), the following equation can be written as

$$I(t) = -\int_s \frac{\sigma}{\rho_0}\nabla \times (M\mathbf{B}_0(\mathbf{r})) \cdot \mathbf{n} dS + \int_s \frac{\sigma}{\rho_0} M\nabla \times \mathbf{B}_0(\mathbf{r}) \cdot \mathbf{n} dS \qquad (9)$$

Furthermore, Equation (9) satisfies $\nabla \times \left(\frac{\sigma}{\rho_0}M\mathbf{B}_0\right) = \nabla\left(\frac{\sigma}{\rho_0}\right) \times M\mathbf{B}_0 + \left(\frac{\sigma}{\rho_0}\right)\nabla \times (M\mathbf{B}_0)$, and the current is expressed as

$$I(t) = -\int_s \nabla \times \left(\frac{\sigma}{\rho_0}M\mathbf{B}_0(\mathbf{r})\right) \cdot d\mathbf{S}(\mathbf{r}) + \int_s \nabla \left(\frac{\sigma}{\rho_0}\right)$$
$$\times M\mathbf{B}_0 \cdot \mathbf{n} dS + \int_s \frac{\sigma}{\rho_0} M\nabla \times \mathbf{B}_0(\mathbf{r}) \cdot \mathbf{n} dS \qquad (10)$$

Simplifying the first part of Equation (10) with Stokes formula, the following equation can be written as

$$I(t) = -\oint_l \frac{\sigma}{\rho_0}M\mathbf{B}_0(\mathbf{r}) \cdot d\mathbf{l} + \int_S \nabla \left(\frac{\sigma}{\rho_0}\right) \times M\mathbf{B}_0(\mathbf{r}) \cdot \mathbf{n} dS$$
$$+ \int_S \frac{\sigma}{\rho_0} M\nabla \times \mathbf{B}_0(\mathbf{r}) \cdot \mathbf{n} dS \qquad (11)$$

where the direction of $d\mathbf{l}$ is shown in Fig. 3.

Considering clinical applications, the ultrasonic transducer emits little energy in the DC frequency range, indicating that the net momentum of the wave packet is zero, so the item $\int_l \frac{\sigma}{\rho_0} M\mathbf{B}_0(\mathbf{r}) d\mathbf{l}$, in Equation (11), is zero.

$$I(t) = \int_S \nabla \left(\frac{\sigma}{\rho_0}\right) \times M\mathbf{B}_0(\mathbf{r}) \cdot \mathbf{n} dS + \int_s \frac{\sigma}{\rho_0} M\nabla \times \mathbf{B}_0(\mathbf{r}) \cdot \mathbf{n} dS \qquad (12)$$

Meanwhile, in the actual detection, the electrode can only detect a portion of the current, and the proportion of the current collected by the signal acquisition system is α. The detection voltage can be expressed as

$$U(t) = \alpha \int_S \nabla \left(\frac{\sigma}{\rho_0}\right) \times M\mathbf{B}_0(\mathbf{r}) \cdot \mathbf{n} dS + \alpha \int_s \frac{\sigma}{\rho_0} M\nabla \times \mathbf{B}_0(\mathbf{r}) \cdot \mathbf{n} dS \qquad (13)$$

It represents the relationship among the voltage measurement, static magnetic field, conductivity, and density of the three-dimensional model.

If the ultrasound generated by the ultrasonic transducer propagates along $\mathbf{e}_x$ direction, the direction of the sound field vibration is $\mathbf{e}_x$ as well. W is the width of the sound field, then dS in Equation (13) can be expressed as $W dx$. The direction of the static magnetic field is $\mathbf{e}_x$, and the magnitude is $B_0(x)$. $\mathbf{J}_0$ is the current density in the cross section which is perpendicular to $\mathbf{e}_y$, thus the direction of $\mathbf{n}$ is $\mathbf{e}_y$. The detected voltage of one-dimensional model in inhomogeneous magnetic field can be derived as

$$U(t) = \alpha W \int_l \frac{\partial}{\partial x}\left(\frac{\sigma}{\rho_0}\right) M B_0(x) dx + \alpha W \int_l \frac{\sigma}{\rho_0}\frac{\partial B_0(x)}{\partial x} M dx \qquad (14)$$

If the static magnetic field is uniform, the detected voltage of one-dimensional model can be derived from Equation (15) as following equation

$$U(t) = \alpha W \int_l \frac{\partial}{\partial x}\left(\frac{\sigma}{\rho_0}\right) M B_0 dx \qquad (15)$$

Equation (16) is consistent with the equation derived by Wen et al. [4].

For biological tissues, assume that the conductivity changes while the density does not change at early stage of the lesion. Equation (15) and Equation (16) can be simplified as

$$U(t) = \frac{\alpha W}{\rho_0}\int_l \frac{\partial \sigma}{\partial x} M B_0(x) dx + \frac{\alpha W}{\rho_0}\int_l \sigma \frac{\partial B_0(x)}{\partial x} M dx \qquad (16)$$

$$U(t) = \frac{\alpha W}{\rho_0}\int_l \frac{\partial \sigma}{\partial x} M B_0 dx \qquad (17)$$

Comparing previous two equations, Equation (16) in inhomogeneous static magnetic field has one more term than Equation (17) with the excitation of uniform static magnetic field. Considering practical applications, the direction of magnetization of static magnetic field is z-direction, and the change of static magnetic field in x-direction is smooth and does not occur abruptly. Hence, the second term of right side of Equation (16) can be ignored. The MAET signal will be amplified or reduced by the factor $\mathbf{B}_0(\mathbf{x})$ at the location where conductivity changes.

From the principle of MAET shown in Equation (16), the relationship between MAET signals and static magnetic field can be used to analyze the characteristics of MAET signal in different static magnetic fields, and it can also be used as a theoretical basis for adjusting MAET signals in inhomogeneous static
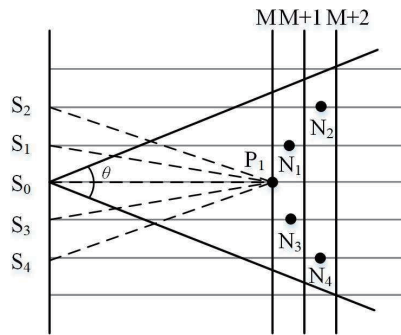
FIGURE 4. Schematic diagram of the principle of synthetic aperture.

magnetic field to signals in uniform static magnetic field. On the other hand, the relationship between the MAET signals and conductivity can be used as a theoretical basis for the qualitative analysis of characteristics of different conductivity regions in synthetic aperture images.

2.2. Synthetic Aperture

Synthetic aperture (SA) is an imaging reconstruction method that uses a small aperture array to move uniformly on a linear trajectory, receiving and storing signals in a determined position sequence [28]. Delay-and-sum (DAS) is a traditional algorithm in SA imaging [29]. According to the spatial position and phase relationship, the coherent superposition of echo signals at different positions is processed to synthesize the matrix of virtual large aperture, so as to obtain the high resolution along the moving direction. In MAET, the MAE signals received by electrodes are generated by ultrasonic excitation, and the MAE signal generated at any point in the target imaging body can be regarded as the ultrasonic signal stimulated by any step point on the stepping path of the ultrasonic transducer to reach the point through delay. After delay superposition, the focusing imaging effect of the target imaging body can be improved.

The MAE signal after delayed superposition is represented as $S_{DAS}(t)$. $S_i(t)$ indicates the MAE signal generated by excitation at different transducer positions. The DAS algorithm is given by Equation (18)

$$S_{DAS}(t) = \sum_i^N S_i(t - \Delta t_i) \tag{18}$$

where Δt_i is the delay time which can be expressed as

$$\Delta t_i = \frac{2z}{c}\left(1 - \sqrt{1 + \frac{(id)^2}{z^2}}\right) \tag{19}$$

where c represents the sound speed, z the vertical distance from the focusing point, and d the displacement step of the transducer.

In Fig. 4, five points in the angular range are involved in the delay superposition, which is the half-power diffusion angle, and the formula is

$$\theta = \sin^{-1}\left(0.71\frac{c}{fl}\right) \tag{20}$$

where f is the ultrasonic frequency, and l is the diameter of the transducer.

Points N_1 and N_3 are between the M and $M+1$ sampling positions. Points N_2 and N_4 are between the $M+1$ and $M+2$ sampling positions. Since the signals S_1, S_3, S_2, and S_4 need to be delayed, the delay coefficients of S_1 and S_3 are α_1, and the delay coefficients of S_2 and S_4 are α_2. α_1 is the 1/sample period, and α_2 is the α_1+1/sample period. The corresponding signals after the delays are shown in Equation (21), respectively.

$$\begin{cases} S_1(N_1) = S_1(M) + \alpha_1\left(|S_1(M+1) - S_1(M)|\right) \\ S_2(N_2) = S_2(M) + \alpha_2\left(|S_2(M+2) - S_2(M+1)|\right) \\ S_3(N_3) = S_3(M) + \alpha_1\left(|S_3(M+1) - S_3(M)|\right) \\ S_4(N_4) = S_4(M) + \alpha_2\left(|S_4(M+2) - S_4(M+1)|\right) \end{cases} \tag{21}$$

The reconstructed signal at position P_1 can be obtained by superimposing the delayed signals of S_1, S_2, S_3, S_4 with S_0

$$S_{DAS}(P_1) = S_0(P_1) + (S_1(N_1) + S_3(N_3)) + (S_2(N_2) + S_4(N_4)) \tag{22}$$

In MAET, the measured electrical signals totalized by applying Equation (22) are used to reconstruct images of the target sample.

3. SIMULATIONS

The simulation model is shown in Fig. 5. The conductivity of the target sample is 0.2 S/m, which represents the normal biological tissue. The conductivity of the ellipsoidal cylinder in the center of the target is 0.5 S/m, which is used as the abnormal pathological biological tissue.

The ultrasound transducer is located at 0.925 cm from the left border of the target sample. When the ultrasonic transducer is in the middle of movement trajectory, there are four locations on the ultrasound propagation path where the conductivity changes, which are ①, ②, ③, and ④ shown in Fig. 5. In the simulation process, the direction of static magnetic field is along the z-axis, and the magnitude of uniform static magnetic field is 300 mT. The inhomogeneous static magnetic field is generated by a single-sided permanent magnet whose length and width are 8.0 cm, and height is 4.0 cm.

As shown in Fig. 6, four boundaries, ①, ②, ③, and ④, where conductivity changes, correspond to the four pulses shown in Fig. 7. Four electrical pulse peaks shown in Fig. 7 are negative,
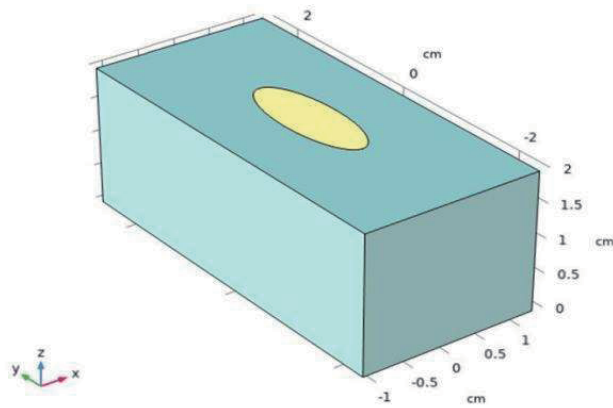
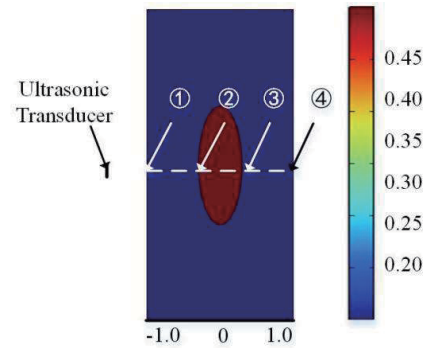FIGURE 5. Three-dimensional simulation model.

FIGURE 6. Tomogram of simulation model.

Detected voltage with uniform static magnetic field excitation
Detected voltage with inhomogeneous static magnetic field excitation
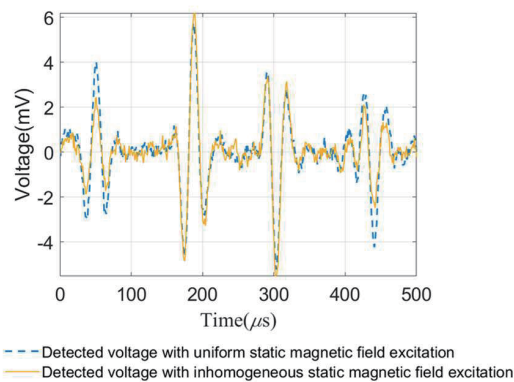
FIGURE 7. Detected voltage with uniform and inhomogeneous static magnetic field excitation.

TABLE 1. Peak values of different pulse of MAET signals in uniform and non-uniform static magnetic fields.

Amplitude of pulse signal	1st	2nd	3rd	4th
Uniform magnetic field (mV)	3.896	6.036	−4.492	−3.918
Non-uniform magnetic field (mV)	2.438	6.237	−5.118	−2.562
Magnitude difference (mV)	1.458	0.201	0.626	1.356
Magnitude difference (%)	37.423	3.313	13.936	34.609

negative, positive, and positive, respectively. Comparing Fig. 6 with Fig. 7, it is shown that electrical signal pulses are generated when the conductivity changes. When the conductivity in the left side of boundaries is smaller than that in the right side, negative peaks will be generated; when the conductivity in the left side of boundaries is larger than that in the right side, positive peaks will be generated. In Fig. 7, the blue dashed line is detected signal under uniform magnetic field with the position of ultrasound transducer at the center axis of the target sample. The yellow line is the detected signal under inhomogeneous magnetic field. The polarity of MAET signal pulses, including positive or negative, obtained from uniform and inhomogeneous static magnetic field excitation corresponds to the direction of conductivity gradient change. Thus, the voltage pulses of MAET can help to distinguish the pathological and

normal regions in both uniform and inhomogeneous static magnetic fields.

The comparison of the peak values of the different pulses of the MAET signals with uniform and inhomogeneous static magnetic field excitation is shown in Table 1. In this table, the peak values of detected voltage pulses in uniform and nonuniform static magnetic field are different, and magnitudes of the changes vary. The smallest change in amplitude reaches as low as 3.313%, and the largest change as high as 37.423%.

With the excitation of 300 mT uniform static magnetic field, the voltage is detected and collected each time when ultrasonic transducer is moving in a straight trajectory. Every time when the position of the ultrasonic transducer changed, the voltage data were obtained. Detected voltage data were formed into a matrix and reconstructed by synthetic aperture imaging method,
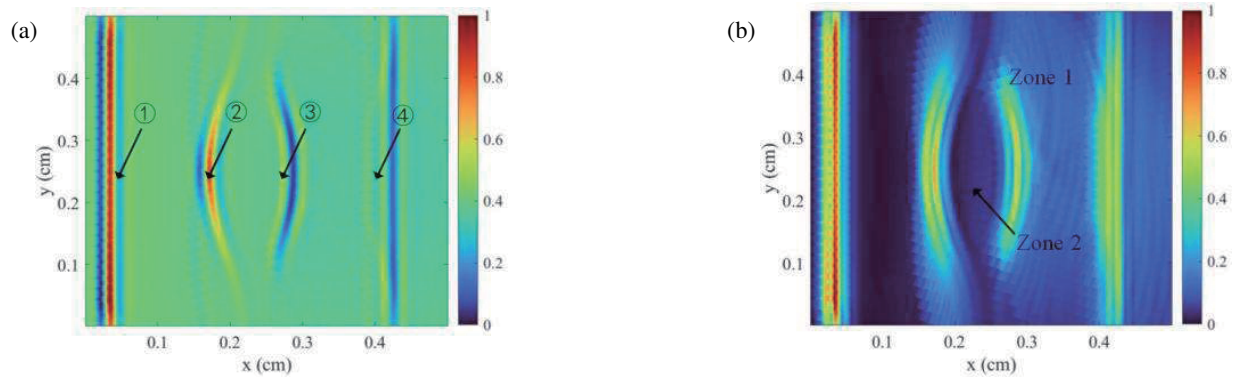
FIGURE 8. Synthetic aperture imaging results of target fault plane. (a) Synthetic aperture imaging result of voltage signals. (b) Synthetic aperture imaging results of signal amplitude.
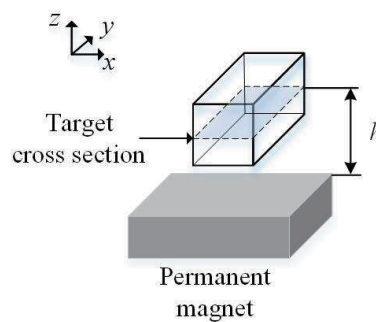

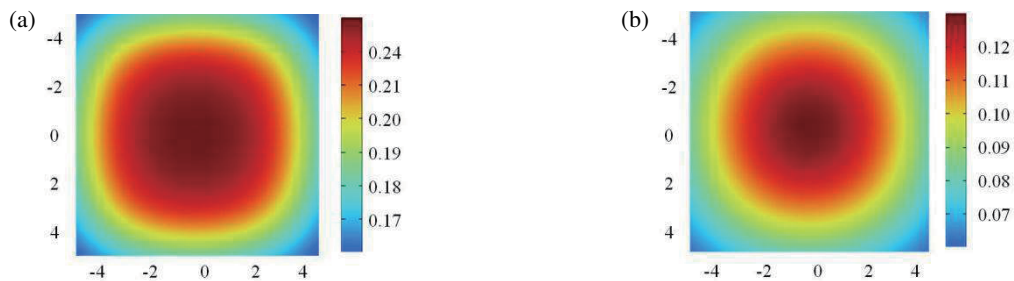**FIGURE 9**. Simulation model and position relationship of single-sided permanent magnet.

FIGURE 10. Magnetic field distribution of unilateral magnets at different distances from the target cross section. (a) $h = 2.0$ cm. (b) $h = 4.0$ cm.

as shown in Fig. 7. In addition, coordinates of color bar in reconstructed images were normalized to 1.

In Fig. 8(a), there are four boundaries in the synthetic aperture imaging, and the four boundaries can correspond to pulse signals in Fig. 7, respectively. There are two regions in Fig. 8(b), where the conductivity of region 1 is σ_1, and the conductivity of region 2 is σ_2. The voltage signals of boundaries ① and ② are negative, indicating that the conductivity of the left side of boundaries ① and ② is smaller than that of the right side; the voltage signals of boundaries ③ and ④ are positive, indicating that the conductivity of the left side of boundaries ③ and ④ is larger than that of the right side. Therefore, the conductivity of region 2 composed of interface ② and interface ③ is larger than the conductivity of region 1.

The positive and negative boundary amplitudes of the partition interface shown in Fig. 9 can reflect the relationship between the magnitude of each anomaly and the background conductivity. When the target sample contains more than one anomaly, the difference in the magnitude of the anomaly boundary can effectively determine the relationship between the conductivity of each anomaly, so the synthetic aperture imaging results combined with the positions and magnitude of signals can reflect the relationship between the magnitude of the background conductivity and the conductivity of the anomaly region.

The inhomogeneous static magnetic field is generated by the single-side permanent magnet, as shown in Fig. 8. When the distance h between the magnet and target cross section is 2.0 cm, the magnetic field distribution at the cross section is shown in Fig. 10(a); the magnetic field distribution at the fault plane when the distance h between the magnet and fault plane is 4.0 cm is shown in Fig. 10(b).
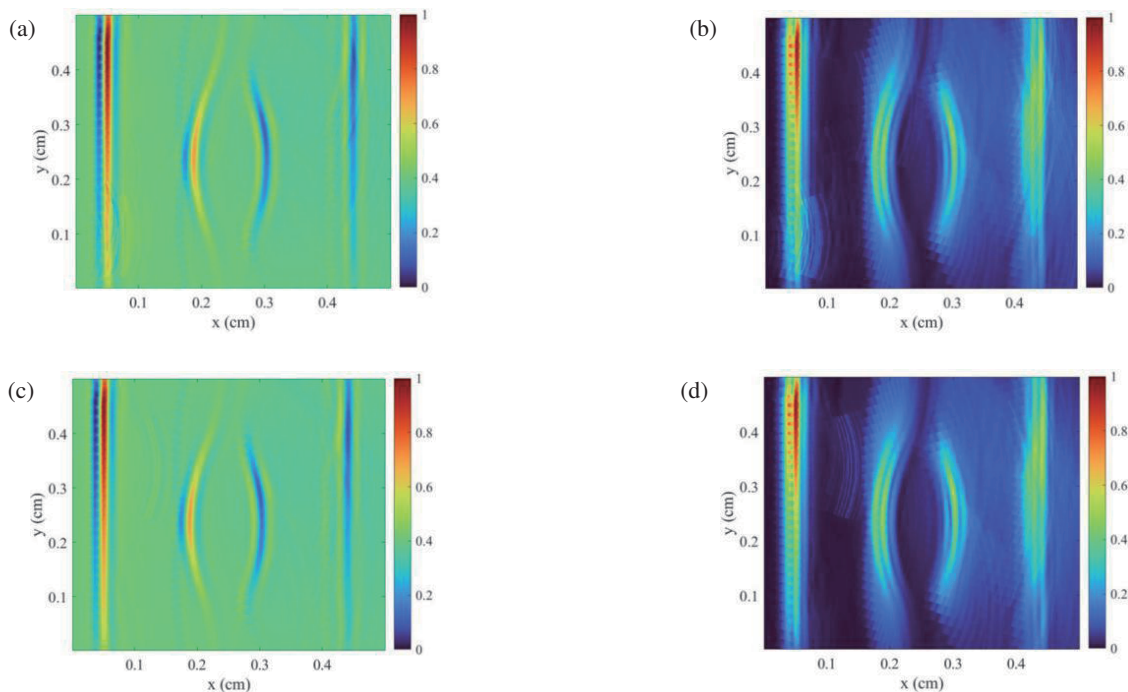
FIGURE 11. Synthetic aperture imaging results in non-uniform static magnetic fields at different distances from a single-side permanent magnet at the target cross section. (a) Synthetic aperture imaging results of the signal in $h = 2.0\,\mathrm{cm}$ plane. (b) Synthetic aperture imaging results of signal amplitude in $h = 2.0\,\mathrm{cm}$ plane. (c) Synthetic aperture imaging results of the signal in $h = 4.0\,\mathrm{cm}$ plane. (d) Synthetic aperture imaging results of signal amplitude in $h = 4.0\,\mathrm{cm}$ plane.

The maximum value of the inhomogeneous static magnetic field distribution shown in Fig. 10(a) is 0.260 T; the minimum value is 0.167 T; and the magnetic field can be expressed as 0.213 ± 0.047 T, with a non-uniformity of 22.1%. The maximum value of the magnetic field shown in Fig. 10(b) is 0.125 T; the minimum value is 0.064 T; and the magnetic field can be expressed as 0.095 ± 0.031 T with a non-uniformity of 32.6%.

When the distance h between the single-side permanent magnet and target cross section is 2.0 cm, and the ultrasonic transducer is scanned along the moving trajectory of a straight line, the synthetic aperture imaging results of the voltage signal and voltage amplitude are obtained as shown in Fig. 11(a) and 11(b), respectively. When the distance h between the single-side permanent magnet and target cross section is 4.0 cm, the synthetic aperture imaging results of the voltage signal and voltage amplitude are obtained as shown in Fig. 11(c) and 11(d), respectively.

Comparing Fig. 11 with Fig. 8, magnitudes corresponding to the boundaries with the same change in conductivity with excitation from inhomogeneous static magnetic field have changed to different degrees. From Fig. 11(b) and 11(d), the boundary magnitudes of the same anomalies are enlarged or reduced by different magnitudes, but it is not possible to distinguish the relationship between the magnitudes of conductivity within each anomalous region based on the difference in magnitudes of the images.

In Figs. 11(b) and 11(d), the magnitude distortion of the synthetic aperture image conductivity partition interface is different when the magnetic field is inhomogeneous. To quantify the magnitude distortion, 2-norm of the error of Figs. 11(b) and 11(d) is calculated respectively. The 2-norm of the error of Fig. 11(b) is 8.715%, and that in Fig. 11(d) is 11.716%.

2-norm of the error can be expressed by following equation

$$RE = \frac{\sqrt{\sum\limits_{i=1}^{N} \sum\limits_{j=1}^{N} \left(I_{u(i,j)} - I_{n(i,j)}\right)^2}}{\sqrt{\sum\limits_{i=1}^{N} \sum\limits_{j=1}^{N} I_{u(i,j)}^2}} \cdot 100\%$$

where $I_{u(i,j)}$ represents the amplitude of point $(i,\ j)$ in the synthetic aperture image of a uniform static magnetic field, and $I_{n(i,j)}$ represents the amplitude of that position of an inhomogeneous static magnetic field.

Equation (16) shows that due to the presence of the inhomogeneous static magnetic field, the magneto-acoustic electric signal at the boundary of the two conductivity variations will be amplified or reduced by the factor $\mathbf{B}_0$. After applying Equation (16), the voltage with inhomogeneous static magnetic field can be corrected, which is shown in Fig. 12. The blue dashed line is the detected signal under uniform magnetic field, and the red line is the detected voltage after correction under inhomogeneous magnetic field. After adjusting, the magnitude of the signal with inhomogeneous static magnetic field is close to the magnitude of voltage with uniform static magnetic field.

Since synthetic aperture image is directly imaged using the magneto-acoustic-electric signal, the conductivity boundaries of tissue in Fig. 13 will also be amplified or reduced by the factor $\mathbf{B}_0$, and will not reflect the conductivity difference between normal biological tissue and abnormal pathological tissue.
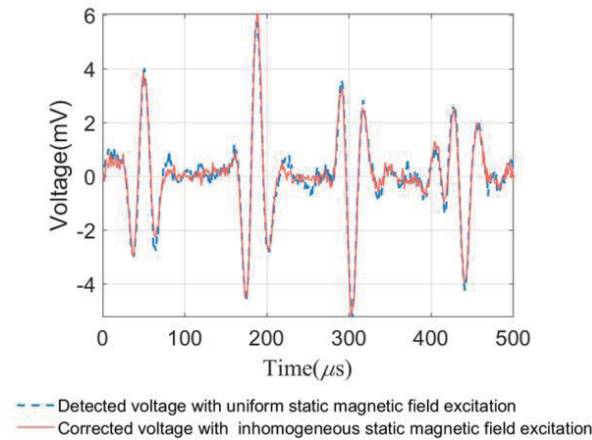
FIGURE 12. Detected voltage with uniform static magnetic field excitation, and corrected voltage with inhomogeneous static magnetic field excitation.
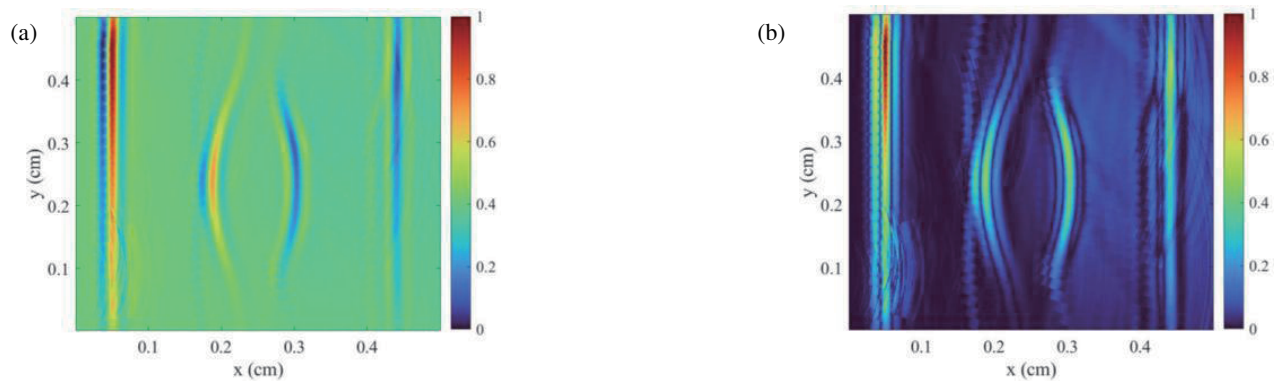

FIGURE 13. Synthetic aperture image under inhomogeneous static magnetic field excitation after correction. (a) Synthetic aperture image of the voltage signal. (b) Synthetic aperture image of voltage amplitude signal.

4. EXPERIMENTS

4.1. Experimental Setup

To conduct experimental studies on phantom and biological tissues, the electrode-detection MAET experimental setup is constructed as shown in the experimental schematic in Fig. 14. The x, y, and z axes in the figure represent the coordinate axes. The electrode-detection MAET experimental system mainly consists of the following three parts.

4.1.1. Pulse Excitation System

Pulse excitation system includes signal generator, power amplifier, ultrasonic transducer, water tank, dielectric oil, and permanent magnet. Signal generator generates voltage signal, which is amplified and transmitted to the ultrasonic transducer by the signal amplifier. The ultrasonic transducer (Panametrics C306, Olympus, USA) is placed in a tank and generates ultrasonic signal at a frequency of 1 MHz. To provide a liquid environment to couple magnetic field and ultrasound field, the water tank was filled with dielectric oil or deionized water, which have the same height as target sample. Target sample and ultrasonic transducer are submerged in the oil or water, and both the center axis of target sample and that of ultrasonic transducer are

kept at the same height. In this paper, it is assumed that the ultrasound propagates at a speed of 1440 m/s uniformly without scattering, reflection, and attenuation of the sound waves. The permanent magnet is placed under the tank to generate inhomogeneous electromagnetic field.

4.1.2. Rotation System

The rotation motor of the system consists of 2 cascaded gears. Gear 1 meshes with gear 2 to drive the ultrasonic transducer to move and rotate through electricity.

4.1.3. MAET Signal Detection System

This detection system includes electrodes A, B, signal acquisition device and oscilloscope. Electrodes A and B are placed on the front and back sides of the target sample, where electrode A is the positive electrode, and electrode B is the negative electrode. Electrical signals obtained from two electrodes are transmitted to the signal acquisition device through wires and conducted to the oscilloscope ultimately.

In this experiment, the target sample is agar phantom, uniformly mixed with sodium chloride solution of 10% mass fraction and agar powder, then heated, and poured into a mold of
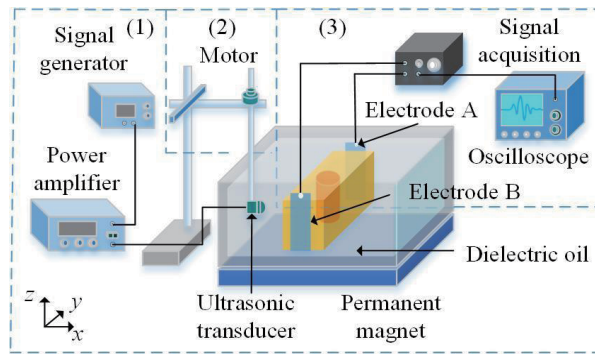
FIGURE 14. Experimental device of electrode-detection MAET in inhomogeneous magnetic field.
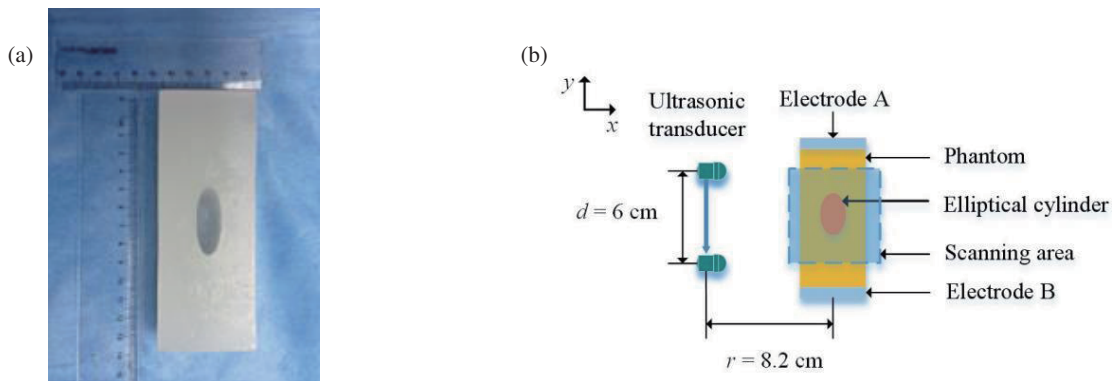

FIGURE 15. Phantom and measurement schematic. (a) Top view of phantom. (b) Measurement schematic of synthetic aperture imaging.

size 4.7 cm*14.3 cm*6.0 cm. After cooling and solidifying, the conductivity of the phantom is 0.5 S/m. The elliptical cylinder, whose long axis is 3.8 cm; short axis is 1.4 cm; and height is 6 cm, placed in the center of the phantom which is hollowed out and injected with dielectric oil. The top view of the phantom is shown in Fig. 14(a).

Synthetic aperture imaging method is used to reconstruct MAET image. The ultrasonic transducer placed on the left side of the target sample emits ultrasound, as shown schematically in Fig. 14(b). The ultrasonic transducer moves along the opposite direction of the y-axis. The distance between the ultrasonic transducer and the center axis of the phantom is 8.2 cm. The scanning step length is 0.03 cm, and 201 sets of data are obtained in total. After each movement of the ultrasonic transducer, it will stay for two seconds to reduce the impact of the transducer's movement on signal acquisition. The distance of the ultrasonic transducer from the center axis of the phantom is 8.2 cm.

Ultrasonic transducer generates signals with amplitude of 400 V and repetition frequency of 1 MHz. The phantom containing sodium chloride generates voltage signals under the action of ultrasound and inhomogeneous magnetic field. Signal acquisition receives voltage signals through electrodes, then displays voltage signal through the oscilloscope to analysis and imaging reconstruction.

4.2. Experiment Results

The top view of phantom is shown in Fig. 15(a). When the ultrasonic transducer in Fig. 15(b) is in the same line with the center of the gel phantom and the elliptical cylinder, the voltage signal detected and displayed by the oscilloscope is shown in Fig. 16.

The first voltage signal fluctuation appeared at about 43 µs, which was close to the time taken for the ultrasound to propagate from the ultrasound transducer to the left boundary of the phantom. The second and third voltage signal fluctuations appeared at 55 µs and 65 µs, respectively, which were nearly the same as the time used for the propagation of the ultrasonic wave from the ultrasonic transducer to the left and right boundaries of the ellipsoidal part inside the phantom. The fourth voltage signal fluctuation appeared at 75 µs, which was similar to the time taken for the ultrasound to propagate from the ultrasonic transducer to the right boundary of the phantom. The time difference between the first and forth voltage signals is about 32 µs. After testing, the propagation speed of ultrasound in the phantom and dielectric oil is about 1440 m/s. Theoretically, the propagation time difference of ultrasound signal generated by the 2 peripheral boundaries of the phantom is $\Delta t = d/v = (4.7\,\text{cm})/(1440\,\text{m/s}) = 32.64\,\mu\text{s}$. Actually, the error includes the measurement error of the distance between the left and right boundaries of the phantom, and the distance from the ultrasonic transducer to phantom. The experimental
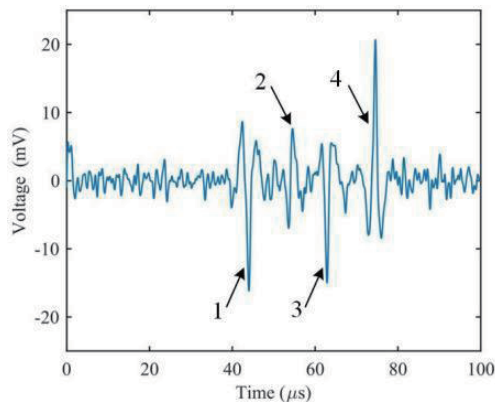
FIGURE 16. Single detection voltage signal.

FIGURE 17. Electrode-detection MAET reconstruction image with synthetic aperture method.

measurement error is $(32.6 - 32)/32.64 \times 100\% = 1.96\%$. It can be assumed that the experimental values are basically consistent with the theoretical ones.

The image of phantom reconstructed by voltage signal in this experiment is shown in Fig. 17. From the reconstructed imaging results, the electrode-detection MAET synthetic aperture method can clearly display the size and shape of the imaging area in the inhomogeneous magnetic field and can detect the change of conductivity of the target sample effectively.

5. CONCLUSIONS

In this paper, MAET in inhomogeneous static magnetic field with synthetic aperture method is proposed. There is no completely uniform static magnetic field in reality. The reconstructed image will introduce an artifact term of magnetic field inhomogeneity, which is small but cannot be ignored. For complex targets, artifacts may be more pronounced and difficult to correct. Therefore, this study has practical clinical application value.

(1) MAET signals in uniform and inhomogeneous static magnetic field are analyzed and compared by simulation. The results show that the amplitude of the MAET pulse signal changes due to the presence of inhomogeneous static magnetic field, and the distortion occurs at the conductivity partition interface in the synthetic aperture imaging results.

(2) Theoretical equations of the MAET under the excitation of inhomogeneous static magnetic field are derived. MAET images based on synthetic aperture are reconstructed in simulations by applying these equations.

(3) Images of conductivity gradient by synthetic aperture in inhomogeneous static magnetic field are verified in experiments. Experiment results reflect the size, shape, and internal conductivity changes of the phantom, which further provides the experimental basis for the practical applications of MAET in nonuniform static magnetic field.
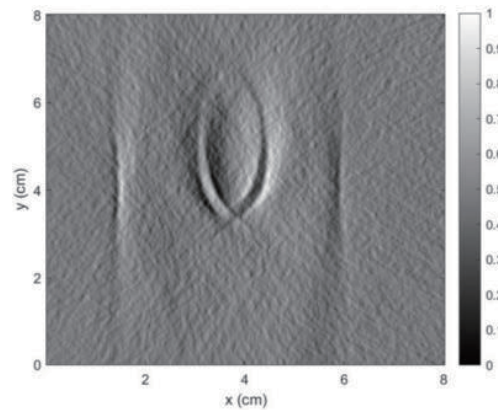
REFERENCES

[1] Gabriel, S., R. W. Lau, and C. Gabriel, "The dielectric properties of biological tissues: II. Measurements in the frequency range 10 Hz to 20 GHz," *Physics in Medicine & Biology*, Vol. 41, No. 11, 2251, 1996.

[2] Grasland-Mongrain, P. and C. Lafon, "Review on biomedical techniques for imaging electrical impedance," *IRBM*, Vol. 39, No. 4, 243–250, Aug. 2018.

[3] Liu, D., D. Smyl, and J. Du, "Nonstationary shape estimation in electrical impedance tomography using a parametric level set-based extended kalman filter approach," *IEEE Transactions on Instrumentation and Measurement*, Vol. 69, No. 5, 1894–1907, May 2020.

[4] Wen, H., J. Shah, and R. S. Balaban, "Hall effect imaging," *IEEE Transactions on Biomedical Engineering*, Vol. 45, No. 1, 119–124, 1998.

[5] Zengin, R. and N. G. Gençer, "Lorentz force electrical impedance tomography using magnetic field measurements," *Physics in Medicine & Biology*, Vol. 61, No. 16, 5887, 2016.

[6] Montalibet, A., J. Jossinet, and A. Matias, "Scanning electric conductivity gradients with ultrasonically-induced lorentz force," *Ultrasonic Imaging*, Vol. 23, No. 2, 117–132, 2001.

[7] Ammari, H., P. Grasland-Mongrain, P. Millien, L. Seppecher, and J.-K. Seo, "A mathematical and numerical framework for ultrasonically-induced lorentz force electrical impedance tomography," *Journal de Mathématiques Pures et Appliquées*, Vol. 103, No. 6, 1390–1409, 2015.

[8] Xu, Y., S. Haider, and A. Hrbek, "Magneto-acousto-electrical tomography: A new imaging modality for electrical impedance," in *13th International Conference on Electrical Bioimpedance and the 8th Conference on Electrical Impedance Tomography*, 292–295, 2007.

[9] Haider, S., A. Hrbek, and Y. Xu, "Magneto-acousto-electrical tomography: A potential method for imaging current density and electrical impedance," *Physiological Measurement*, Vol. 29, No. 6, S41, 2008.

[10] Renzhiglova, E., V. Ivantsiv, and Y. Xu, "Difference frequency magneto-acousto-electrical tomography (DF-MAET): Application of ultrasound-induced radiation force to imaging electrical current density," *IEEE Transactions on Ultrasonics, Ferroelectrics, and Frequency Control*, Vol. 57, No. 11, 2391–2402, 2010.

[11] Zeng, X., G. Liu, H. Xia, and X. Xu, "An acoustic characteristic study of magneto-acousto-electrical tomography," *2010 3rd International Conference on Biomedical Engineering and Informatics*, Vol. 1, 95–98, 2010.

[12] Guo, L., G.-Q. Liu, H. Xia, Y. Liu, and M.-H. Lu, "Conductivity reconstruction algorithms and numerical simulations for magneto-acousto-electrical tomography with piston transducer in scan mode," *Chinese Physics B*, Vol. 23, No. 10, 104303, 2014.

[13] Guo, L., G. Liu, and H. Xia, "Magneto-acousto-electrical tomography with magnetic induction for conductivity reconstruction," *IEEE Transactions on Biomedical Engineering*, Vol. 62, No. 9, 2114–2124, 2015.

[14] Grasland-Mongrain, P., F. Destrempes, J.-M. Mari, R. Souchon, S. Catheline, J.-Y. Chapelon, C. Lafon, and G. Cloutier, "Acousto-electrical speckle pattern in lorentz force electrical impedance tomography," *Physics in Medicine & Biology*, Vol. 60, No. 9, 3747, 2015.

[15] Kunyansky, L., C. P. Ingram, and R. S. Witte, "Rotational magneto-acousto-electric tomography (MAET): Theory and experimental validation," *Physics in Medicine & Biology*, Vol. 62, No. 8, 3025, 2017.

[16] He, Y., "Theoretical and experimental research of inductive magneto-acoustic coupling imaging based on ultra-fast active detection technology," M.S. thesis, School of Biomedical Engineering, Shenzhen Univ., 2017.

[17] Dai, M., X. Chen, T. Sun, L. Yu, M. Chen, H. Lin, and S. Chen, "A 2D magneto-acousto-electrical tomography method to detect conductivity variation using multifocus image method," *Sensors*, Vol. 18, No. 7, 2373, 2018.

[18] Kaboutari, K., A. O. Tetik, E. Ghalichi, M. S. Gözü, R. Zengin, and N. G. Gençer, "Data acquisition system for maet with magnetic field measurements," *Physics in Medicine & Biology*, Vol. 64, No. 11, 115016, 2019.

[19] Sun, T., P. Hao, C. T. Chin, D. Deng, T. Chen, Y. Chen, M. Chen, H. Lin, M. Lu, Y. Gao, S. Chen, C. Chang, and X. Chen, "Rapid rotational magneto-acousto-electrical tomography with filtered back-projection algorithm based on plane waves," *Physics in Medicine & Biology*, Vol. 66, No. 9, 095002, 2021.

[20] Sun, Z., G. Liu, H. Xia, and S. Catheline, "Lorentz force electrical-impedance tomography using linearly frequency-modulated ultrasound pulse," *IEEE Transactions on Ultrasonics, Ferroelectrics, and Frequency Control*, Vol. 65, No. 2, 168–177, 2018.

[21] Li, Y., G. Liu, H. Xia, and Z. Xia, "Numerical simulations and experimental study of magneto-acousto-electrical tomography with plane transducer," *IEEE Transactions on Magnetics*, Vol. 54, No. 3, 1–4, 2018.

[22] Li, Y., G. Liu, Z. Sun, H. Xia, and Z. Xia, "Magneto-acousto-electrical tomography for high resolution electrical conductivity contrast imaging," *Journal of Medical Imaging and Health Informatics*, Vol. 8, No. 7, 1402–1407, 2018.

[23] Li, Y., J. Song, H. Xia, and G. Liu, "The experimental study of mouse liver in magneto-acousto-electrical tomography by scan mode," *Physics in Medicine & Biology*, Vol. 65, No. 21, 215024, 2020.

[24] Li, C., Y. Li, and G. Liu, "Simulation of lung tissue imaging based on magneto-acousto-electrical technology," *Diangong Jishu Xuebao/Transactions of China Electrotechnical Society*, Vol. 36, No. 4, 732–737, 2021.

[25] Deng, D., T. Sun, L. Yu, Y. Chen, X. Chen, M. Chen, S. Chen, and H. Lin, "Image quality improvement of magneto-acousto-electrical tomography with barker coded excitation," *Biomedical Signal Processing and Control*, Vol. 77, 103823, 2022.

[26] Li, P., W. Chen, G. Guo, J. Tu, D. Zhang, and Q. Ma, "General principle and optimization of magneto-acousto-electrical tomography based on image distortion evaluation," *Medical Physics*, Vol. 50, No. 5, 3076–3091, 2023.

[27] Li, Y., S. Bu, X. Han, H. Xia, W. Ren, and G. Liu, "Magneto-acousto-electrical tomography with nonuniform static magnetic field," *IEEE Transactions on Instrumentation and Measurement*, Vol. 72, 1–12, 2023.

[28] Moreira, A., P. Prats-Iraola, M. Younis, G. Krieger, I. Hajnsek, and K. P. Papathanassiou, "A tutorial on synthetic aperture radar," *IEEE Geoscience and Remote Sensing Magazine*, Vol. 1, No. 1, 6–43, Mar. 2013.

[29] Holmes, P. M., H.-K. Lee, and M. W. Urban, "F-number optimization for synthetic aperture delay-multiply-and-sum reconstruction," *Ultrasonics*, Vol. 136, 107158, Jan. 2024.